JOURNAL OF AIRCRAFT
Vol. 44, No. 4, July–August 2007

Residual Stress/Strain in Three-Row, Countersunk, Riveted Lap Joints

Gang Li,* Guoqin Shi,† and Nicholas C. Bellinger‡
National Research Council, Ottawa, Ontario K1A 0R6, Canada

DOI: 10.2514/1.26748

The stress/strain variations from the riveting process to the tensile loading stage in lap joints with three-row countersunk rivets were studied experimentally and numerically. Three different forces were used in the riveting process. After releasing the rivet squeeze forces, the lap joints were then loaded in tension. Three-dimensional finite element models were developed to simulate the experimental setup. The material elastoplastic constitutive relationship and geometric nonlinear properties, as well as nonlinear contact boundary conditions, were included in the numerical simulations. The numerical modeling techniques were validated using experimental data. The effect of the residual stress on the stress variations along a prescribed path during the tensile loading stage is discussed. Full-field contours of the maximum principal stress during the tensile loading stage are also analyzed. The aim of this research is to develop an accurate three-dimensional numerical technique to study the complex stress and strain distributions induced by the entire loading sequence and to use this information to more accurately predict the fatigue life of fuselage lap joints.

Nomenclature

C	=	material parameter
D	=	rivet-shank diameter
D_{hole}	=	inner-sheet hole diameter
$D_{\max}$	=	maximum rivet-shank diameter after riveting
E, E'	=	Young's modulus under plane stress and strain conditions, $E' = E/(1 - v^2)$
H_o	=	rivet protruding height above the inner-sheet surface before riveting
I	=	moment of inertia about the sheet-bending neutral axis
M_0	=	bending moment at the overlap end
m	=	material parameter
t	=	joint sheet thickness
v	=	Poisson's ratio
W	=	joint sheet width
ε	=	normal strain
$\varepsilon_{\text{true}}$	=	true strain
σ	=	normal stress
σ_{true}	=	true stress beyond the initial yield stress
σ_y	=	initial yield stress

I. Introduction

FUSELAGE lap joint integrity is significantly influenced by the residual stress and strain in the hole vicinity induced by the riveting process [1–7]. The magnitudes of the induced residual stress and strain are directly related to the rivet squeeze force [1,5,8,9]. Secondary bending is generated due to the eccentricity of the load path when the riveted lap joints are loaded in tension [10,11]. The residual stress/strain field, joint configuration, and secondary bending make the stress/strain in the hole vicinity very different from the remote tensile stress/strain conditions [11].

With the success of the study of single-row, countersunk, riveted lap joints [11–13], further investigation of the effects of residual stress/strain on the stress/strain variations during the tensile loading stage for lap joints with three-row countersunk rivets was carried out. This work is the extension of a project carried out at the Institute for Aerospace Research to study the residual stress induced by the riveting process [8,11–14]. Because the three-row, countersunk, riveted lap joints are typically used for fuselage structures in the aircraft rather than the single-row riveted lap joints, the study of the stress condition in this kind of lap joint is of practical importance.

A literature review [1–15] showed that there was little information available on three-row lap joints during the entire loading sequence that included the following aspects: 1) the relationship between the rivet squeeze force and residual stress and strain, 2) the influence of the residual stress on the stress variations during the tensile loading stage, and 3) the experimental strain measurement during the entire loading sequence, from the riveting process to the joint tensile loading stage.

In this paper, three different rivet squeeze forces (10-, 14-, and 18-kN) were used to install rivets in lap joints. After riveting, the lap joints were loaded in tension to a maximum remote stress of 98.6 MPa [10–13]. The main objective of this work is to develop the three-dimensional numerical simulation capability, to provide insightful stress and strain states in the fastener-hole vicinity, and to use the stress and strain information to more accurately predict the fatigue life of fuselage lap joints.

II. Experimental Details

A. Joint-Coupon and Strain-Gauge Information

A total of three joint specimens were tested [16]. Each joint consisted of two 1.60-mm-thick Al 2024-T3 alloy bare sheets, riveted with three Al 2117-T4 alloy, countersunk-type, MS20426AD5-6 rivets. Joint configuration and dimensions are given in Fig. 1 and Table 1. The mean clearance between the rivet and hole was 0.06 mm. Tabs with dimensions of $50 \times 25.4 \times 1.60$ mm were bonded to the ends of each joint, to eliminate the initial secondary bending moment that would be induced when the joints were installed in the load frame.

Microstrain gauges made by Measurements Group were used to capture the strain variations during the test [8,12–14,16]. Gauges 1 to

Presented as Paper 2269 at the 47th AIAA/ASME/ASCE/AHS/ASC Structures, Structural Dynamics, and Materials Conference, Newport, RI, 1–4 May 2006; received 24 July 2006; revision received 19 January 2007; accepted for publication 22 January 2007.

*Associate Research Officer, Structures and Materials Performance Laboratory, Institute for Aerospace Research, 1200 Montreal Road; Gang.Li@nrc-cnrc.gc.ca. Member AIAA (Corresponding Author).

†Senior Research Officer, Structures and Materials Performance Laboratory, Institute for Aerospace Research, 1200 Montreal Road. Member AIAA.

‡Structures Group Leader, Structures and Materials Performance Laboratory, Institute for Aerospace Research, 1200 Montreal Road. Member AIAA.

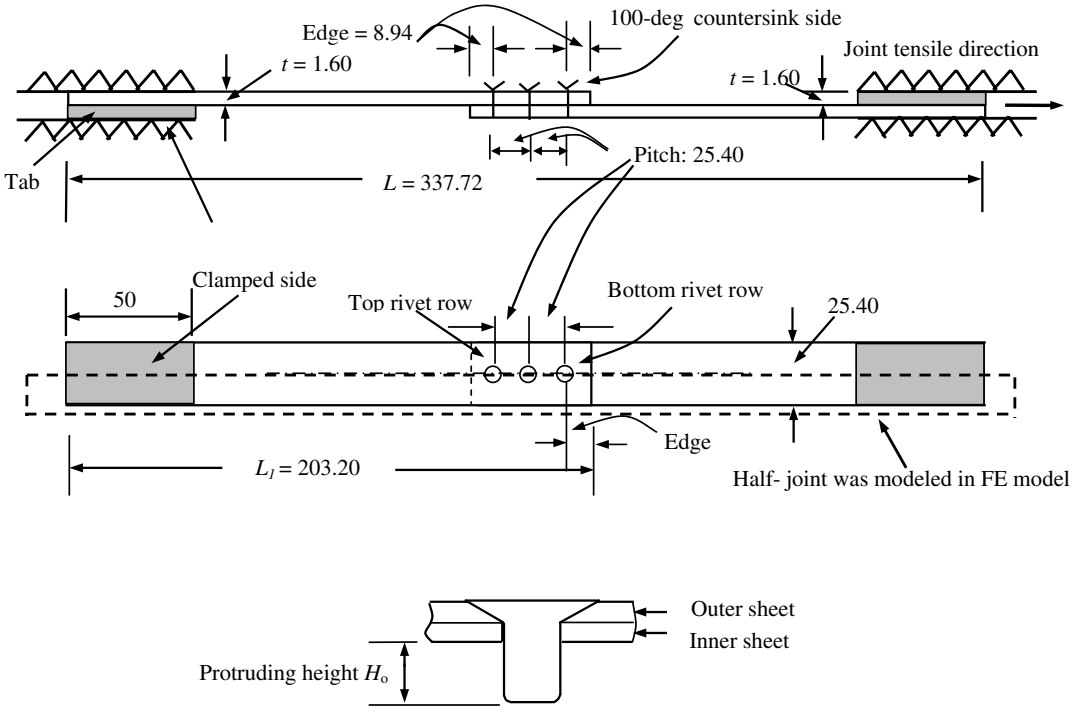

Fig. 1 Diagram of the lap joint with three countersunk rivets, mm.

4 were mounted on the inner-sheet surface before riveting to capture the strain variation during the riveting process. Gauges 5 to 15 were mounted after riveting. All the microstrain gauges were positioned in the joint's longitudinal (joint's tensile) direction, as shown in Fig. 2. Microstrain gauges 1, 2, 3, 5, 7, and 8 were the MM EA-13-031DE-350 type, with a gauge factor of $2.06 \pm 1.0\%$ and transverse sensitivity of $(1.2 \pm 0.2)\%$ at 24°C. Microstrain gauges 4, 6, and 9 to 15 were the MM EA-13-031EC-350 type, with a gauge factor of $2.09 \pm 1.0\%$ and transverse sensitivity of $(0.4 \pm 0.2)\%$ at 24°C. Gauges 1 to 3 were used to measure the strain values in the hoop direction, and gauge 4 was used to measure the radial strain during the riveting process. All of the gauges were reset to zero and then used to measure the longitudinal strain variations during the tensile loading stage. Gauges 5 to 8, on the outer-sheet surface, were near the fastener holes. Secondary bending, at the overlap end, was estimated from the strain values in gauges 9 and 10. Gauge 11 was used to measure the far-field strain. Gauges 12 to 15 were mounted at the rivet pitch center to analyze the load transmission information between the outer and inner sheets.

To avoid possible damage to the strain gauges by the large rivet driven-head deformation and difficulties in gauge setup, gauges 1 to 4 were mounted more than 2.5 mm away from the hole edge. Tables 2–4 give these microstrain-gauge locations. The gauges were in good condition and also well-calibrated before and after mounting. Because these gauges were not within the hole vicinity and the joint's maximum remote tensile stress was less than one-third of the sheet's initial yield stress, the measured strains were much less than the strain-gauge limit of approximately 3%. Thus, the influences of the gauges' transverse sensitivity and nonlinearity on the measured strains were not considered. Each strain-gauged specimen was tested under one of the three different rivet squeeze forces [16]. The coordinate-frame origin position is at the middle fastener-hole center, and the microstrain-gauge position was relative to its nearby fastener-hole-center location. Only the strain results obtained from the joint, riveted using the 18-kN squeeze force, were compared with the corresponding numerical predictions in this paper. Strain comparisons for the joints riveted using the 10- and 14-kN squeeze forces are summarized elsewhere [17].

B. Testing Equipment and Loading Condition

Lap-joint specimens were riveted and then loaded in tension using a 250-kN MTS Load Frame with serial number 455 and model number 311.11.

To avoid both thermal and inertial effects on the material properties, a small constant-load ramp of 111.2 N/s was chosen for all the rivet installations [8,12–14]. This is much slower than that used in the actual riveting process. Three rivets were installed one by one, starting from the center rivet. To keep the same riveting condition for each coupon, the coupons were held firmly to a mobile heavy metal plate. Gauges were reset to zero before the next riveting process to avoid any potential disturbances to both gauge and coupon. After riveting, the joints were then loaded in tension to a maximum remote stress of 98.6 MPa [10–13,16,17]. The tensile loading rate was 0.5 mm/min [18]. These measured data were used to validate the numerical predictions.

III. Finite Element Simulations

A. Material Parameters

Because of the joint symmetry, only half of the joint (Fig. 1) was modeled. Symmetric boundary conditions were applied to the joint center plane along the longitudinal x direction.

The material parameters used were the same as ones used in a previous analysis [8,11–14,16,17]. An isotropic hardening behavior was assumed for both the rivet and sheet materials. The material constants C and m were determined using the curve-fitting method by substituting the uniaxial tensile test data [19] into Equation (1):

Table 1 Joint dimensions based on optical measurements of the three specimens

Sheet dimensions, mm	Distance between the panel side edge and the nearby hole center, mm	Mean D_{hole}, mm	Mean H_o, mm	D, mm
203 × 25.4 × 1.60	8.94	4.09	6.06	3.97

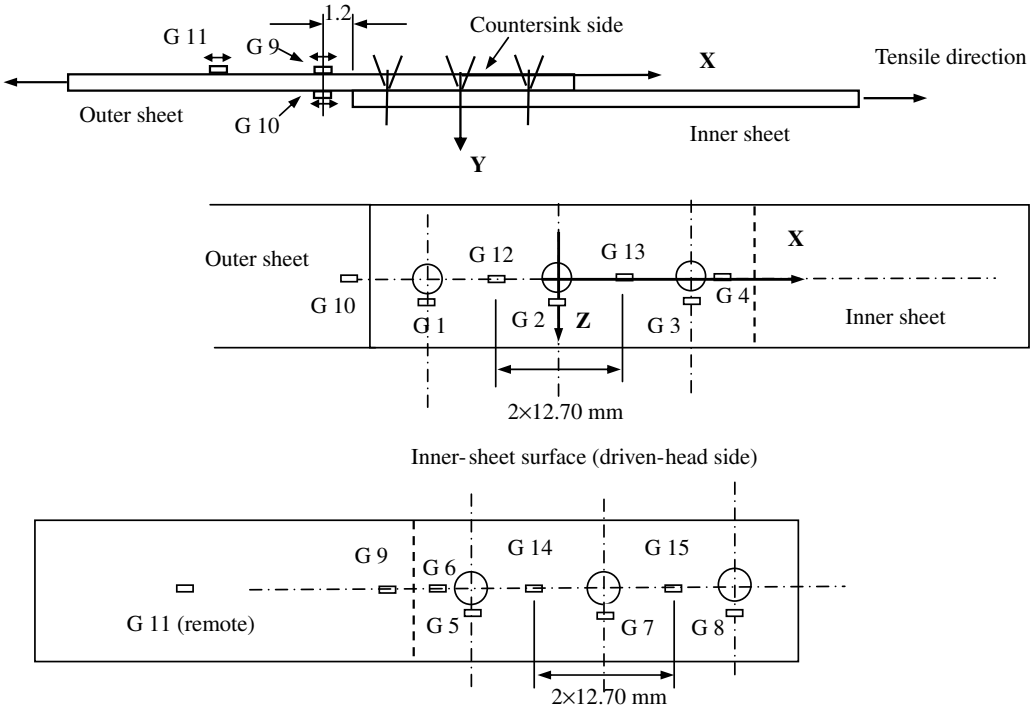

Fig. 2 Microstrain-gauge arrangements in a joint coupon (not to scale).

$$\sigma_{\text{true}} = C(\varepsilon_{\text{true}})^m \tag{1}$$

The true stress and plastic strain values were entered into the table provided by the MSC.Patran interface, which uses linear interpolation for values between the points to implement the hardening behavior in the model.

Material parameters for the 2117-T4 Al alloy MS20426AD5-6 rivet [5,8,11–14,17,20] and 2024-T3 Al alloy bare sheet [8,11–14,17,19,20] are summarized in Tables 5 and 6, respectively.

B. Finite Element Modeling

The finite element (FE) model was generated in accordance with the experimental joints using the FE software packages MSC.Patran (pre- and postprocessor) version 2004r2 and MSC.Marc (solver) version 2001. A total of 12,362 nodes and 9,096 eight-node, three-dimensional, reduced-integration brick elements (type 117) were used, and the three-dimensional FE model is shown in Fig. 3. Element type 117 is an eight-node isoparametric arbitrary hexahedral for general three-dimensional applications using

Table 2 Locations (mm) of the microstrain gauges 1 to 4 (Fig. 2)

	Gauge location on the joint's inner-sheet surface			
	Gauge 1	Gauge 2	Gauge 3	Gauge 4
Rivet squeeze force, kN	z position (±0.4)[a] (absolute value)			x position (±0.4)[a]
18	6.1	6.2	6.5	6.5

[a]The gauge length was around 0.8 mm and the table values were measured between the hole-center and the gauge-center positions.

Table 3 Locations (mm) of the microstrain gauges 5 to 8 (Fig. 2)

	Gauge location on the joint's inner-sheet surface			
	Gauge 5	Gauge 7	Gauge 8	Gauge 6
Rivet squeeze force, kN	z position (±0.4)[a] (absolute value)			x position (±0.4)[a]
18	6	6	6	6

[a]The gauge length was around 0.8 mm and the table values were measured between the hole-center and the gauge-center positions.

Table 4 Locations (mm) of the microstrain gauges 9 to 15 (Fig. 2)

	Gauge location on the joint's inner-sheet surface			
	Gauges 9 and 10	Gauge 11	Gauges 12 and 14	Gauges 13 and 15
Rivet squeeze force, kN	To overlap edge		At the pitch center position	
18	1.2	42	25.4	25.4

Table 5 Elastic and plastic properties for 2117-T4 Al alloy MS20426AD5-6 rivet material

Parameter of rivet	Value
Young's modulus	71.7 GPa
Poisson's ratio	0.33
Initial yield stress	172 MPa
Hardening parameters when $0.02 \leq \varepsilon_{true} \leq 0.10$	$C = 544$ MPa and $m = 0.23$
Hardening parameters when $0.10 < \varepsilon_{true} \leq 1.0$	$C = 551$ MPa and $m = 0.15$

Table 6 Material parameters for 1.60-mm-thick 2024-T3 Al alloy bare sheet

Parameter of 2024-T3 Al alloy bare sheet	Value
Young's modulus	72.4 GPa
Poisson's ratio	0.33
Initial yield stress	310 MPa
True ultimate stress	552 MPa
Hardening parameters when $\varepsilon_y \leq \varepsilon_{true} \leq 0.02$	$C = 676$ MPa and $m = 0.14$
Hardening parameters when $0.02 < \varepsilon_{true} \leq 0.1$	$C = 745$ MPa and $m = 0.164$
Slope of linear hardening curve when $\varepsilon_{true} > 10\%$	1034 MPa

reduced integration. This element uses an assumed strain formulation written in natural coordinates that insures good representation of the shear strains in the element and is preferred over high-order elements when used in a contact analysis [21].

Five deformable contact bodies (two sheets and three rivets) and four rigid contact bodies (three pushers and one rigid set) were defined in the model. The rigid set contacted the joint's bottom surface. Three rigid pushers were used to squeeze the three rivets' driven heads. Specific contact pairs for both surface to surface and point to point were not needed, because the current finite element software package could handle this particular contact situation if it occurred. A friction coefficient of 0.2 was used in the Coulomb model for all contact surfaces. A force-controlled riveting method was used in this numerical study. The same squeeze force was used to install all three rivets in one joint [16,17]. The rivet squeeze forces used in the FE model were half the value used for the experiments, due to the simulation of the half-joint.

Multiple load steps, with their specific boundary conditions, were defined in one entire loading sequence. Load step 1 applied the squeeze force to the center pusher to squeeze the center rivet; load step 2 released the squeeze force back to zero at the center rivet; load step 3 applied the squeeze force to the top rivet pusher, which squeezed the top rivet; load step 4 released the squeeze force back to zero at the top rivet; load step 5 applied the squeeze force to the lower rivet pusher, which squeezed the lower rivet; load step 6 released the squeeze force back to zero at the lower rivet; and load step 7 applied the in-plane loading to the joint, up to a maximum stress of 98.6 MPa. In the final load step, the three deformable bodies contacted each other and the rigid bodies were deactivated [17].

1. Displacement Boundary Conditions Used in the 3-D FE Model

As shown in Fig. 3, the following displacement boundary conditions were used during the riveting process:

Set 1: $U_y = U_z = 0$ was at the remote edges of the joint.

Set 2: $U_x = U_z = 0$ was applied to the center rivet axis.

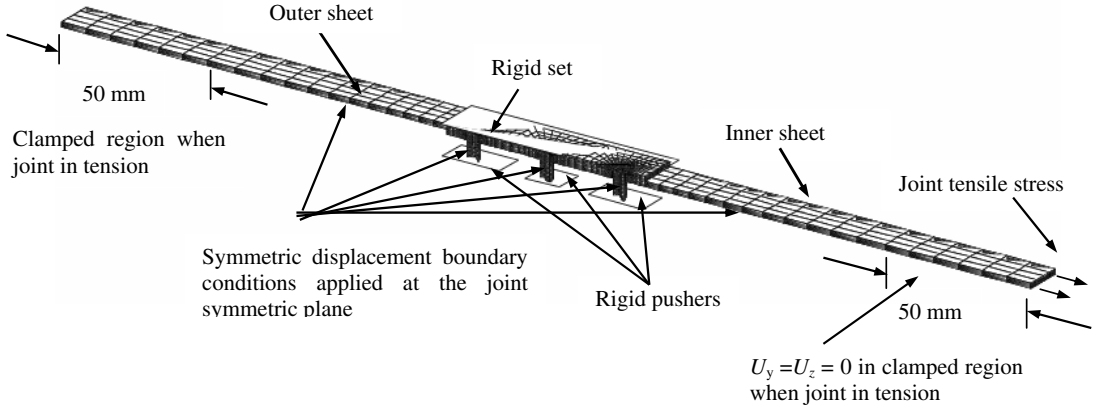

a) Three-dimensional FE model

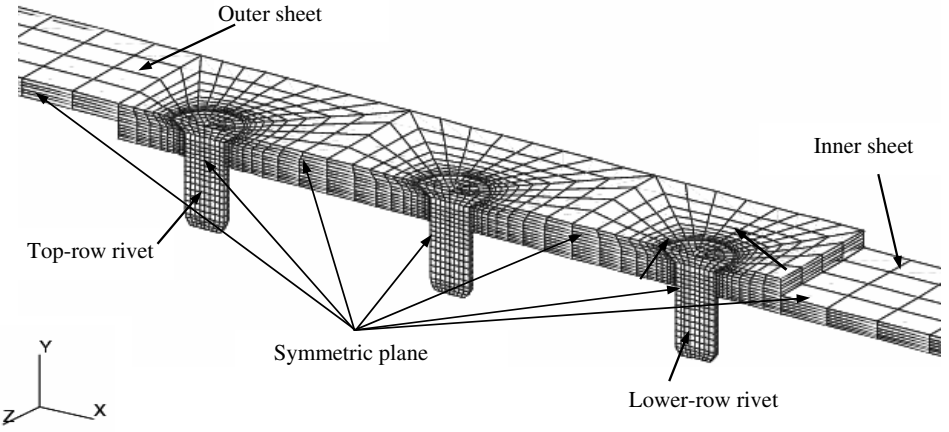

b) Overlap region after removal of four rigid bodies

Fig. 3 The three-dimensional finite element model for the lap joints meshed using a total of 9,096 eight-node reduced-integration brick elements and 12,362 nodes.

Table 7 Contact pairs defined in the numerical job

Load steps	Purpose of load step	Specific contact pairs used	Modification
1 and 2	Install the center rivet	Inner sheet to three rivets, inner sheet to outer sheet, outer sheet to three rivets, outer sheet to rigid set, three rivets to rigid set, and center rivet to center rigid pusher	——
3 and 4	Install the top-row rivet	Inner sheet to three rivets, inner sheet to outer sheet, outer sheet to three rivets, outer sheet to rigid set, three rivets to rigid set, and top-row rivet to top rigid pusher	The pair "center rivet to center pusher" was deactivated and a new pair (top-row rivet to top rigid pusher) was defined
5 and 6	Install the lower-row rivet	Inner sheet to three rivets, inner sheet to outer sheet, outer sheet to three rivets, outer sheet to rigid set, three rivets to rigid set, and lower-row rivet to lower rigid pusher	The pair "top rivet to top pusher" was deactivated and a new pair (lower-row rivet to lower rigid pusher) was defined
7	Load up the remote tensile stress	Inner sheet to three rivets, inner sheet to outer sheet, and outer sheet to three rivets	All the rigid bodies were deactivated

Set 3: $U_z = 0$ was applied at the joint's longitudinal center (symmetric) plane.

The influence of the boundary conditions (at the far ends of the joint, set 1) on the stress and strain distributions in the hole vicinity during the riveting process can be ignored, based on Saint-Venant's principle [22].

The following displacement boundary conditions were used in the tensile loading stage after releasing the squeeze forces:

Set 4: The displacements $U_x = U_y = U_z = 0$ were applied at the left far end of the joint for a length of 50 mm. The length of the clamped joint end was 50 mm in the experiments.

Set 5: Displacements $U_y = U_z = 0$ were applied at the right far end of the joint for a length of 50 mm, and the joint was loaded in tension in the longitudinal x direction.

Set 6: $U_z = 0$ was applied at the joint's longitudinal center (symmetric) plane in the longitudinal direction (x axis).

2. *Contact Pairs Used in the Numerical Job*

During the riveting process, the contact areas were 1) the faying surface between the inner and outer sheets, 2) the area between the inner sheet and rivets, 3) the area between the outer sheet and rivets, 4) the area between the rivets' driven heads and the rigid pushers, and 5) the area between the rivets and the rigid supporting surface. During the tensile loading stage after the riveting process, the contact areas were the areas between the inner sheet, outer sheet, and rivets only.

For the numerical simulations, the single-sided contact-detection method was used. Contact pairs were defined in each load step, as given in Table 7.

IV. Results And Discussion

A. Joint Deformations

Comparisons of the experimental and numerical results for the rivets' driven-head deformations are summarized in Table 8. Large rivet squeeze forces induced large driven-head deformations. The relative difference between the experimental and numerical results for the driven-head deformation of $D_{\max}/D$ was within 2%. Rivet driven-head deformations, obtained from the experimental [16] and numerical results, are shown in Figs. 4 and 5. Good agreement was achieved for the rivet driven-head deformation from the numerical simulations.

Table 8 Rivet deformations of $D_{\max}/D$ obtained from the experimental and finite element analysis (FEA) results

Rivet squeeze force, kN	Test $D_{\max}/D$ [16]	FEA $D_{\max}/D$
10	1.31	1.32
14	1.50	1.52
18	1.63	1.66

B. In Situ Quantitative Comparisons Between the Experimental and Numerical Results

1. *Riveting Process*

Because of the distance between the rivets, the riveting process did not influence the adjacent holes [16,17]. To have a clear comparison of hoop-strain variation during the riveting process, the experimental average hoop strains for gauges 1 to 3 [$\varepsilon_{\text{avg}} = (\varepsilon_{G1} + \varepsilon_{G2} + \varepsilon_{G3})/3$] were used, because they were located at similar positions relative to their neighboring holes. Comparisons of the average hoop strain from gauges 1 to 3 and the radial strain from gauge 4 during the riveting process are presented in Fig. 6. After releasing the rivet squeeze force, the measured residual strain was approximately

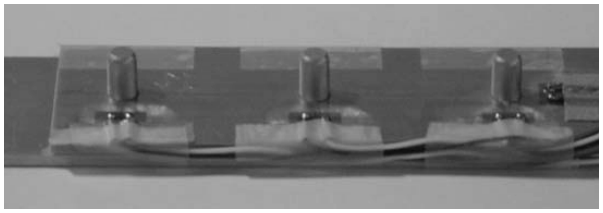

a) Before riveting

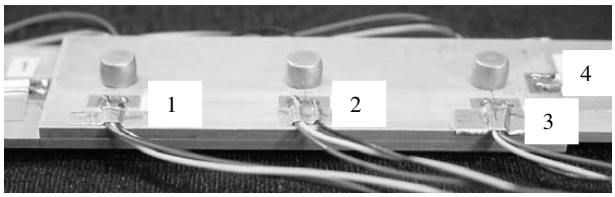

b) Riveted by the 10-kN rivet squeeze force

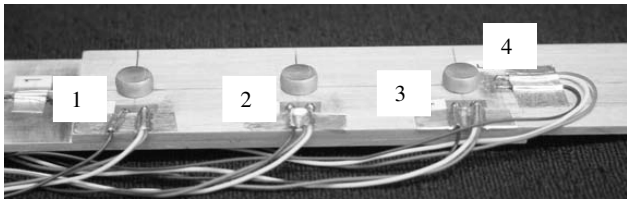

c) Riveted by the 14-kN rivet squeeze force

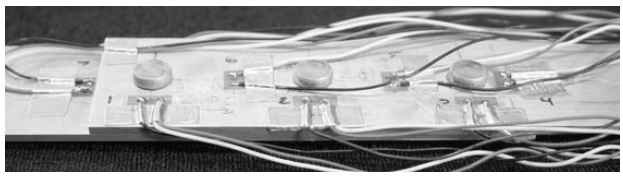

d) Riveted by the 18-kN rivet squeeze force

Fig. 4 Photographs of the MS20426AD5-6 rivets' driven-head deformations in the lap joints after the riveting process, using different rivet squeeze forces.

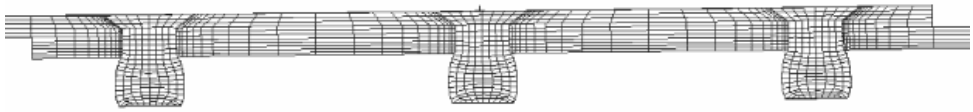

a) Joint was loaded in tension to 98.6 MPa after the riveting process using the 10-kN squeeze force

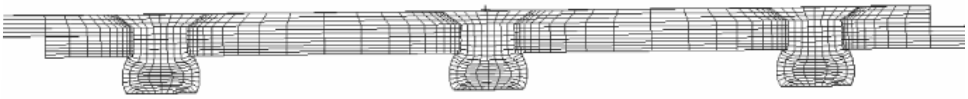

b) Joint was loaded in tension to 98.6 MPa after the riveting process using the 14-kN squeeze force

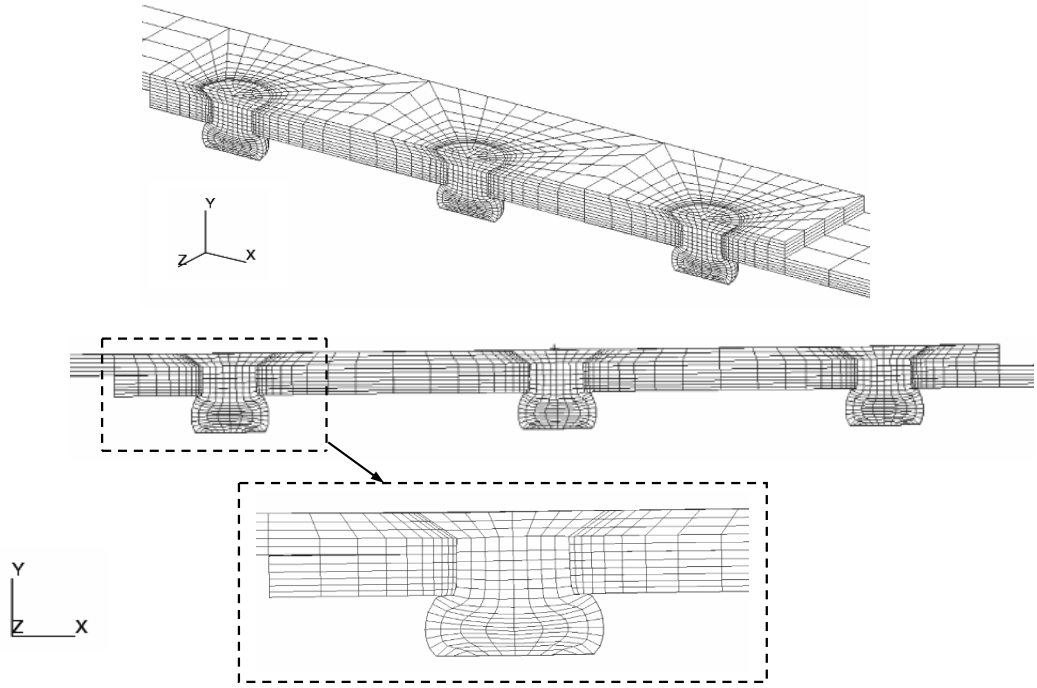

c) Joint was loaded in tension to 98.6 MPa after the riveting process using the 18-kN squeeze force

Fig. 5 Lap-joint deformations during the tensile loading stage after the riveting process; no penetrations occurred.

0.175% in gauge 1, 0.131% in gauge 2, and 0.118% in gauge 3. The closer the gauge position was to the hole, the greater the residual strain that was generated. Tensile hoop strain and compressive radial strain were observed during the riveting process. A small elastic recovery was observed in the radial direction from the numerical simulations. A similar trend, without the evident strain reversal, can be observed from the experimental results. The reversal strain occurred in previous test results [12–15], which could have resulted from the clearance that was present between the sheet/rivet hole interface and the rivet standing position (distance of the rivet head above the sheet surface) during the riveting process. Generally, the difference between the numerical predictions and experimental results is smaller after riveting. For example, a large difference in gauge 4, radial strain, occurred at the squeeze force of approximately 8 kN during the riveting process, and the difference was approximately 9% after riveting.

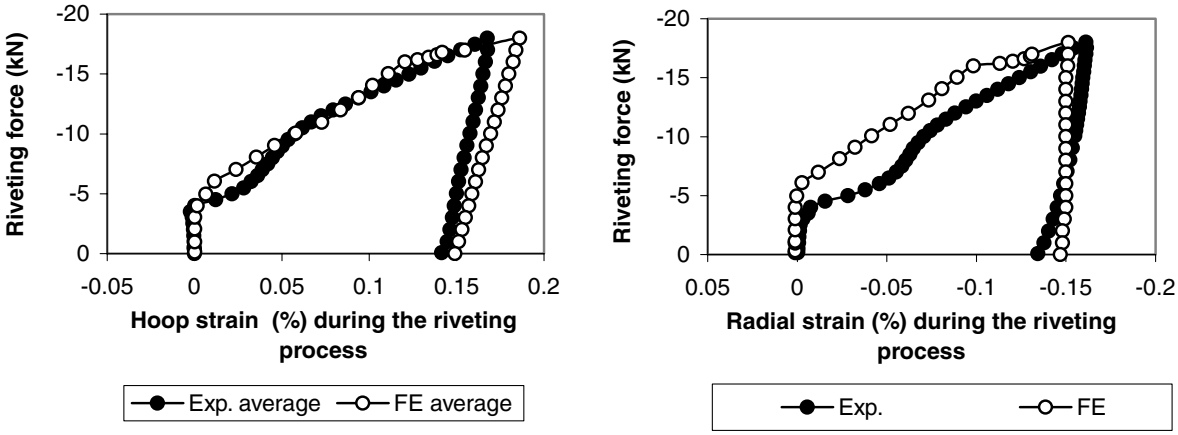

a) Average hoop strain of gauges 1 to 3

b) Radial strain in gauge 4

Fig. 6 Comparison of the variations of the hoop and radial strains on the joint's inner surface during the riveting process using the 18-kN rivet squeeze force.

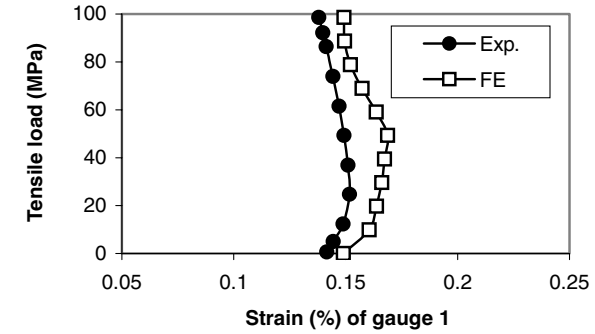

a) gauge 1

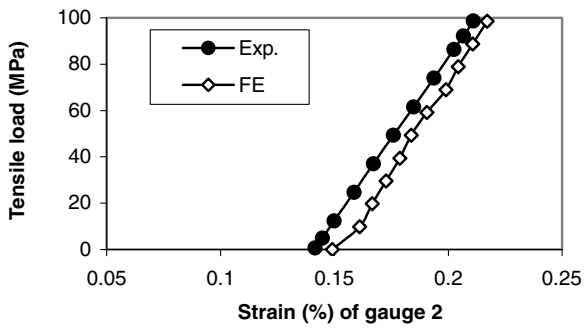

b) gauge 2

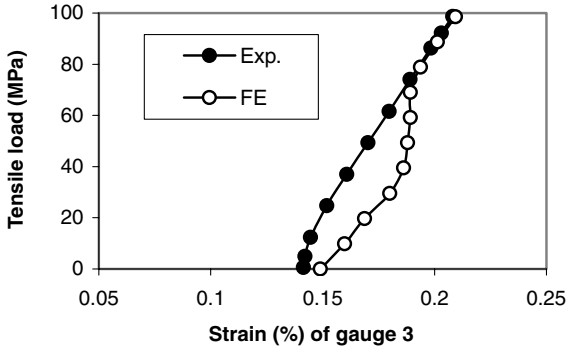

c) gauge 3

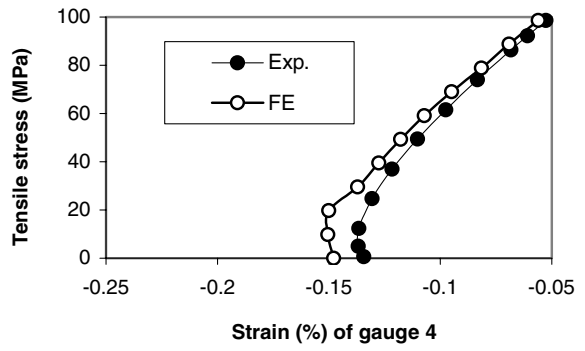

d) gauge 4

Fig. 7 Comparison of the strain variations in the gauges 1 to 4 joints during the tensile loading stage after releasing the 18-kN rivet squeeze force.

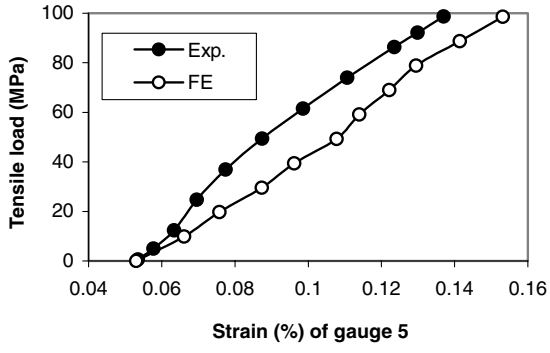

a) gauge 5

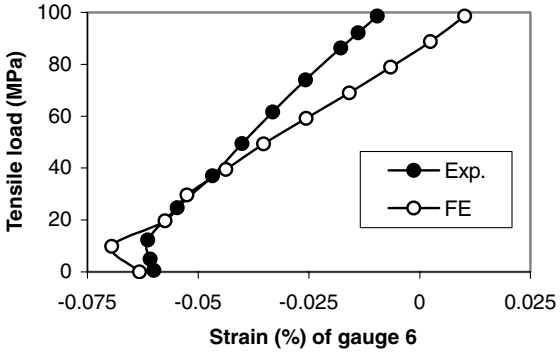

b) gauge 6

Fig. 8 Comparison of the strain variations in gauges 5 and 6 during the tensile loading stage after releasing the 18-kN rivet squeeze force.

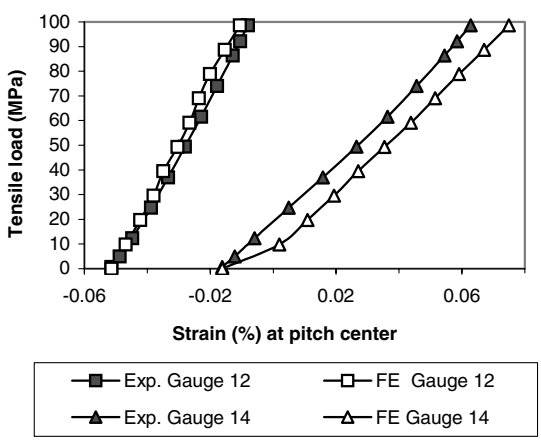

a) Centre between top and center rivet rows

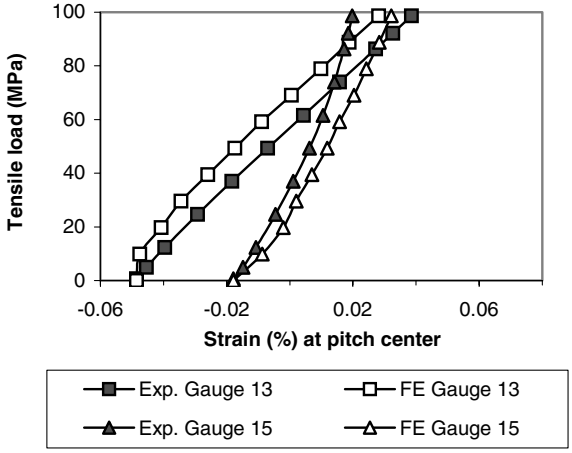

b) Centre between center and bottom rivet rows

Fig. 9 Comparison of the strain variations in gauges 12 and 14 and gauges 13 and 15 at the pitch center during the tensile loading stage after releasing the 18-kN rivet squeeze force.

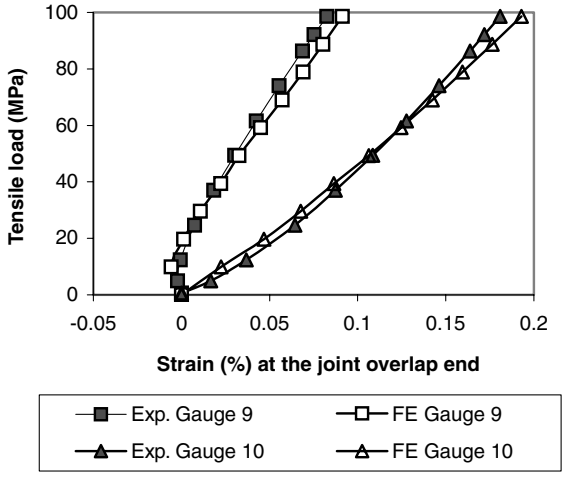

Fig. 10 Comparison of the strain variations in gauges 9 and 10 at the overlap end during the tensile loading stage after releasing the 18-kN rivet squeeze force.

2. Comparisons of Strain Variations During the Tensile Loading Stage

Quantitative strain comparisons during the tensile loading stage were further carried out to validate the numerical results. To compare the experimental and numerical results, the experimentally measured residual strains were used as the starting values for gauges 1 to 4 during the tensile loading stage. For other gauges that were mounted after riveting, the residual strain values obtained from the numerical simulations were the starting values in these gauges during the tensile loading stage. To be consistent, the average residual strain ε_{avg} will be further used as the initial value for gauges 1 to 3 during the tensile loading stage.

As shown in Fig. 2, gauges 5 and 6 were mounted on the outer-sheet surface near the top rivet row, and gauges 7 and 8 were near the center and lower rivets. Strain variations in gauges 7, 8, and 11 were not as crucial as in gauges 5 and 6, and thus these results are not present in this paper.

Gauge 1 was on the inner sheet near the top rivet row and showed that the tensile hoop strain initially increased and then slightly decreased with the increment of tensile load (Fig. 7). This result was dominantly influenced by the joint's secondary bending. Variation trends obtained from the experimental and numerical results in gauge 3 were slightly different when the remote tensile stress was between 0 and 60 MPa, after which the results compared very well. The reason for this discrepancy could be the numerical error.

Strain variations in gauges 5 and 6 during the tensile loading stage, obtained from the experimental and numerical results, are presented in Fig. 8. The starting values for gauges 5 and 6 during the experimentally tensile loading stage were obtained from the numerical results. Similar positions existed in gauges 3 and 5, as well as in gauges 4 and 6. However, strain variations in these gauges were different at the beginning of the tensile load. Moreover, ranges of strain variation during the tensile loading stage for gauges 3 and 5 were similar, whereas those for gauges 4 and 6 were clearly different. These observations would be caused by several reasons: 1) different hole shape, 2) different clearance between the sheet and rivet, and 3) different bending stress/strain induced by secondary bending for both the inner and outer sheets.

Gauges 12 to 15 were mounted along the pitch centerline. Strain variations in gauges 12 to 15, obtained from the experimental and numerical results, are presented in Fig. 9. If the residual strains were not included, the difference magnitude between these results for gauges 12 and 14 was almost identical to the difference between gauges 13 and 15, which describes the load-transmission condition between the two sheets. The transferred load from the inner to the outer sheet in the area between the top rivet row to the center rivet row was the same as the load transferred from the outer to the inner sheet in the area between the center rivet row to the bottom rivet row.

Strain gauges 9 and 10 were mounted near the joint overlap to estimate the secondary bending moment. Comparison of the longitudinal strain variations for the two gauges, between the

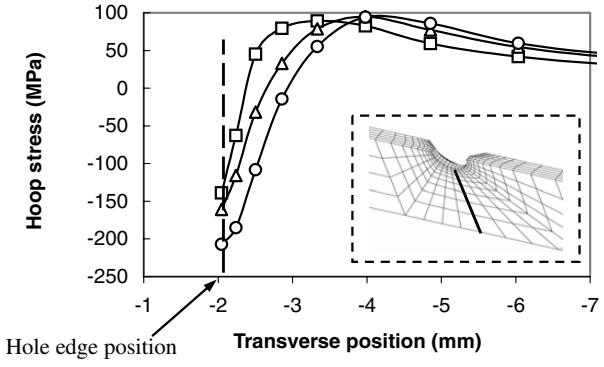

a) Remote tensile stress of 0 MPa

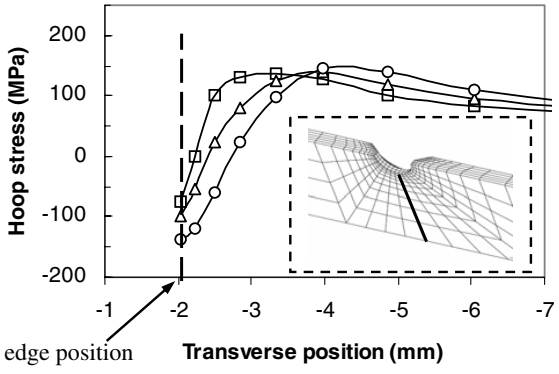

b) Remote tensile stress of 49.3 MPa

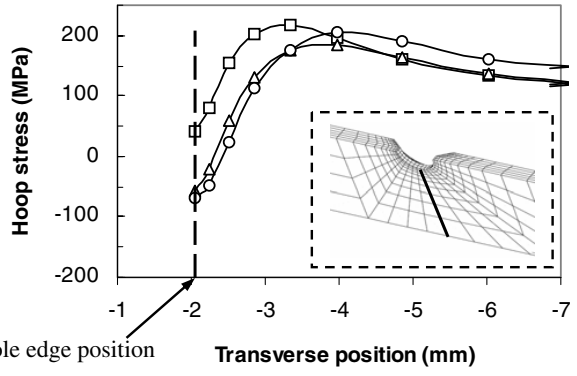

c) Remote tensile stress of 98.6 MPa

Fig. 11 Hoop-stress variations along the transverse path during the tensile loading stage after releasing the □ 10-kN, △ 14-kN, and ○ 18-kN rivet squeeze forces.

experimental and numerical results, is presented in Fig. 10. Good agreement was achieved between the experimental and numerical results. The relative differences between the numerical and experimental strain results were approximately 10% in gauge 9 and 6% in gauge 10 when the remote tensile stress was 98.6 MPa. The bending moment at the joint overlap end can be estimated using the obtained strain values. The normal stress at the outer-sheet surface caused by bending can be obtained using the following expression [23]:

$$\sigma_{\text{bending}} = \frac{\sigma_{G10} - \sigma_{G9}}{2} = E_{\text{sheet}}\left(\frac{\varepsilon_{G10} - \varepsilon_{G9}}{2}\right) \quad (2)$$

Bending moment at the overlap end can then be estimated as [23]

$$M_0 = \frac{\sigma_{\text{bending}} I}{t/2} = \frac{W(t^3/12)\sigma_{\text{bending}}}{t/2} = \frac{E_{\text{sheet}} W t^2}{12}(\varepsilon_{G10} - \varepsilon_{G9}) \quad (3)$$

where E_{sheet} is the sheet Young's modulus. The bending moment in Eq. (3) was calculated under plane-stress conditions. To obtain the bending moment under plane-strain condition, Young's modulus E should be replaced by E' [$E' = (E/1 - v^2)$].

Generally, good agreements were achieved in each strain pair comparisons between the experimental and numerical results, as shown in Figs. 6–10. It could be drawn from these strain comparisons that the residual stress, induced by the riveting process and stress conditions during the joint's tensile loading stage, could be analyzed using the current numerical results with reasonable accuracy.

The discrepancy between the experimental and FE model predictions could be explained by the following: 1) inaccuracies in the constitutive models beyond yielding for the sheet and rivet used in the FE model, 2) perfect assumptions made for the material properties and perfect geometry surface, 3) differences in how the strain values were obtained: the strain was determined from a point/node in the FE model, whereas it was averaged over the gauge area for the experiments, 4) numerical errors in the FE model, for example, insufficiently refined finite element meshes, and 5) errors associated with the strain gauge, for example, gauge reliability and gauge mount conditions.

C. Hoop-Stress Variations Along the Prescribed Transverse Path

The magnitude of the hoop-stress conditions in the top fastener-hole vicinity along a transverse path on the outer-sheet faying surface could be used to indicate the effect induced by the riveting process. Because the strain gauges could not be mounted in the fastener-hole vicinity, the hoop-stress variations were numerically studied during the tensile loading stage. This path was at the top rivet row perpendicular to the joint's longitudinal tensile direction.

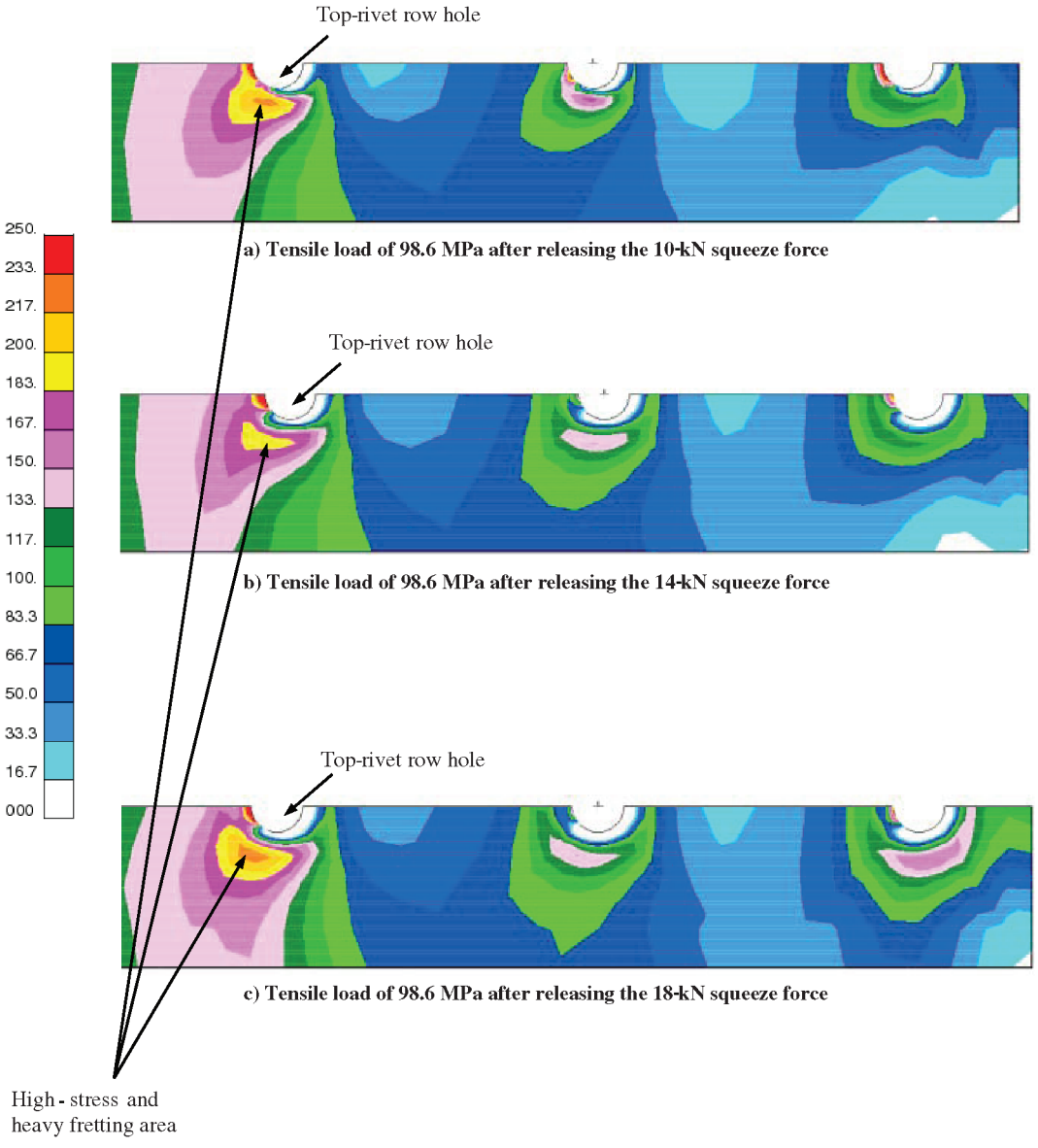

Fig. 12 Maximum principal stress (MPa) on the outer-sheet faying surface when the joints were loaded in tension.

The hoop-stress variations, considering the influence of the rivet squeeze force, are presented in Fig. 11. The following characteristics can be observed from this figure:

1) A large rivet squeeze force generated a large compressive hoop stress.

2) Nonlinear variations in the hoop stress occurred during the tensile loading stage.

The results in this figure showed that the residual stresses induced by the rivet squeeze force had considerable effect on the stress variations during the tensile loading stage. For example, comparing with the residual hoop stress at the hole edge induced by the riveting process using the 10-kN rivet squeeze force, the decrease in the residual hoop-stress magnitude was approximately −16% for the case using the 14-kN rivet squeeze force and −49% for the case using the 18-kN rivet squeeze force. When the joint's remote tensile stress was 98.6 MPa, the corresponding increments of the hoop-stress magnitude were approximately 128, 58, and 50% using the three different rivet squeeze forces of 10 kN, 14 kN, and 18 kN.

D. Full-Field Stress Contours

The full-field stress distributions can provide insightful information. The maximum principal stress during the tensile loading stage was chosen. The maximum principal stress is of great importance in the study of crack nucleation during the tensile loading stage. The crack usually occurs on the outer-sheet faying surface, due to the heavy fretting damage that can occur. The corresponding full-field stress contours were on the outer-sheet faying surface, highlighting the overlap region. Residual hoop, radial, and minimum principal stresses induced by the riveting process are given elsewhere [17].

Figure 12 shows the maximum principal stress condition on the outer-sheet faying surface when the joints were loaded in tension to a maximum remote stress of 98.6 MPa. It was found from this figure that

1) The distribution area and shape of the maximum principal stress shifted to the holes' upper side.

2) Large maximum principal stress mainly occurred at the top-rivet-row hole region.

3) A large rivet squeeze force moved the high-stressed region away from the holes' edge vicinity.

The large maximum principal stress distribution area and shape were consistent with the experimental fatigue testing results [24]. In the fatigue tests of noncorroded joints, cracks typically originated in the outer-sheet heavily fretted area around the upper-rivet hole a short distance away from the top-rivet hole edge [24]. Increasing the riveting force increases the contact area around all the rivets, and thus the load transfer in each row is more efficient.

V. Conclusions

Both experimental and numerical studies of the lap joints with three-row countersunk-type rivets were carried out from the riveting process to the tensile loading stage. A three-dimensional finite element model was developed. In situ strain values were measured using microstrain gauges during the entire loading sequence. Good agreement was achieved between the experimental results and numerical predictions in the entire loading sequence. The residual stress and strain induced by the riveting process, as well as the stress and strain variations during the tensile loading stage, considering the effects of the residual stress/strain, were numerically investigated.

Consistent and compatible behaviors of the hoop-stress variations along the prescribed transverse path on the outer sheet were observed when the tensile load was up to 98.6 MPa. The residual stress was significantly affected by the riveting process, which in turn affected the stress state during the tensile loading stage. Large rivet squeeze forces moved the high maximum principal stress away from the joint-hole vicinity.

The numerical results showed that high-strength lap joints could be fabricated using a relatively large rivet squeeze force to install rivets. Residual compressive stress, induced by the riveting process, effectively decreased the stress concentration in the fastener-hole vicinity.

Acknowledgments

The financial assistance received from the Department of National Defence/Defence Research and Development Canada (DND/DRDC) is gratefully acknowledged. This work was also partially supported by the Institute for Aerospace Research (IAR) and Analysis Process/Engineered Solution (APES), Inc. collaboration on fretting fatigue program (project 46_QJ0_39). This work was carried out under IAR Program 303 Aerospace Structures (project 46_QJ0_37), Residual Stresses in Riveted Lap Joints. Our sincere acknowledgement to J. P. Komorowski and G. Eastaugh for their valuable discussions, suggestions, and help in the research. Many thanks to those people who have in one way or another contributed to the work.

References

[1] Müller, R. P. G., "An Experimental and Analytical Investigation on the Fatigue Behavior of Fuselage Riveted Lap Joints," Ph.D. Thesis, Faculty of Aerospace Engineering, Delft Univ. of Technology, Delft, South Holland, The Netherlands, Oct. 1995.

[2] Donaldson, D. R., and Kenworthy, K. J., "Fatigue Design and Test Program for the American SST," *Aircraft Fatigue Design, Operational and Economics Aspects*, edited by J. Y. Mann, and I. S. Milligan, Pergamon, Rushcutters Bay, NSW, Australia, 1972, pp. 437–476.

[3] Hazlehurst, L., and Woods, M., "Automated Rivet Interference Inspection System," Society of Automotive Engineers Paper 941842, 1994.

[4] Fung, C P., and Smart, J., "Riveted Single Lap Joints. Part 1: A Numerical Parametric Study," *Proceedings of the Institution of Mechanical Engineers, Part G (Journal of Aerospace Engineering)*, Vol. 211, No. 1, 1997, pp. 13–27.

[5] Szolwinski, M. P., and Farris, T. N., "Linking Riveting Process Parameters to the Fatigue Performance of Riveted Aircraft Structures," *Journal of Aircraft*, Vol. 37, No. 1, 2000, pp. 130–137.

[6] Trego, A., and Cope, D., "Evaluation of Damage Tolerance Analysis Tools for Lap Joints," *AIAA Journal*, Vol. 39, No. 12, 2001, pp. 2250–2254.

[7] Mackerle, J., "Finite Element Analysis of Fastening and Joining: A Bibliography (1990–2002)," *International Journal of Pressure Vessels and Piping*, Vol. 80, No. 4, 2003, pp. 253–271.

[8] Li, G., and Shi, G., "Effect of the Riveting Process on the Residual Stress in Fuselage Lap Joints," *Canadian Aeronautics and Space Journal*, Vol. 50, No. 2, 2004, pp. 91–105.

[9] Terada, H., "A Proposal on Damage Tolerant Testing for Structural Integrity of Aging Aircraft—Learning from JAL Accident in 1985," edited by F. Erdogan, *Fracture Mechanics: 25th Volume*, ASTM STP 1220, American Society for Testing and Materials, Philadelphia, 1995, pp. 557–574.

[10] Bellinger, N. C., Komorowski, J. P., and Benak, T. J., "Residual Life Prediction of Corroded Fuselage Lap Joints," *International Journal of Fatigue*, Vol. 23, Supplement 1, 2001, pp. S349–S356.

[11] Li, G., and Shi, G., "Evaluation of the Numerical Modeling Results in Simulating the Fuselage Lap Joints with Single Countersunk Type Rivet," Inst. for Aerospace Research, National Research Council Paper LM-SMPL-2004-0118, 2004.

[12] Li, G., Shi, G., and Bellinger, N. C., "Studies of Residual Stress in Single Row Countersunk Riveted Lap Joints," 46th AIAA/ASME/ASCE/AHS/ASC Structures, Structural Dynamics, and Materials Conference, AIAA Paper 2005-2024, 2005.

[13] Li, G., Shi, G., and Bellinger, N. C., "Studies of Residual Stress in Single Row Countersunk Riveted Lap Joints," *Journal of Aircraft*, Vol. 43, No. 3, 2006, pp. 592–599.

[14] Li, G., Shi, G., and Bellinger, N. C., "Studies of Residual Strain in Lap Joints," *Journal of Aircraft*, Vol. 43, No. 4, 2006, pp. 1145–1151.

[15] Langrand, B., Patronelli, L., Deleotombe, E., Markiewicz, E., and Drazetic, P., "An Alternative Numerical Approach for Full Scale Characterization for Riveted Joint Design," *Aerospace Science and Technology*, Vol. 6, No. 5, 2002, pp. 343–354.

[16] Li, G., and Shi, G., "Experimental Investigation of Residual Strains in Lap Joints with Three Row Countersunk Rivets," Inst. for Aerospace Research, National Research Council Paper LM-SMPL-2005-0042, 2005.

[17] Li, G., Shi, G., and Bellinger, N. C., "Numerical Investigation of Residual Stress/Strain Conditions in Lap Joints with Three Row Countersunk Rivets," Inst. for Aerospace Research, National Research Council Paper LTR-SMPL-2005-0045, 2005.

[18] Li, Q. M., Mines, R. A. W., and Birch, R. S., "Static and Dynamic Behaviour of Composite Riveted Joints in Tension," *International Journal of Mechanical Sciences*, Vol. 43, No. 7, 2001, pp. 1591–1610.

[19] Li, G., and Shi, G., "Investigation of Residual Stress in Riveted Lap Joints: Experimental Study," Inst. for Aerospace Research, National Research Council Paper LTR-SMPL-2003-0099, 2003.

[20] "Metallic Materials and Elements for Aerospace Vehicle Structures" [CD ROM], U.S. Department of Defense, Rept. MIL HDBK 5H, Dec. 1998.

[21] "MARC Volume B: Element Library, Version K7," MARC Analysis Research Corp., Palo Alto, CA, 1997.

[22] Timoshenko, S. P., and Goodier, J. N., *Theory of Elasticity*, McGraw–Hill, New York, 1970.

[23] Li, G., and Lee-Sullivan, P., "Experimental Research and Finite Element Method Analysis of Balanced Single Lap Joints Under Tension," *International Journal of Adhesion and Adhesives*, Vol. 21, No. 3, 2001, pp. 211–220.

[24] Eastaugh, G. F., Straznicky, P. V., Krizan, D. V., Merati, A. A., and Cook, J., "Experimental Study of the Effects of Corrosion on the Fatigue Durability and Crack Growth Characteristics of Longitudinal Fuselage Splices," *Aging Aircraft 2000* [CD ROM], Warner Robins Air Logistics Center, Robins AFB, GA, 2000